Driven optical matter: Dynamics of electrodynamically coupled nanoparticles in an optical ring vortex

Patrick Figliozzi,[1] Nishant Sule,[2] Zijie Yan,[2,*] Ying Bao,[2] Stanislav Burov,[2,†] Stephen K. Gray,[3] Stuart A. Rice,[1,2] Suriyanarayanan Vaikuntanathan,[1,2] and Norbert F. Scherer[1,2,‡]

[1]*Department of Chemistry, The University of Chicago, Chicago, Illinois 60637, USA*

[2]*James Franck Institute, The University of Chicago, Chicago, Illinois 60637, USA*

[3]*Center for Nanoscale Materials, Argonne National Laboratory, Lemont, Illinois 60439, USA*

(Received 24 October 2016; revised manuscript received 26 December 2016; published 13 February 2017)

To date investigations of the dynamics of driven colloidal systems have focused on hydrodynamic interactions and often employ optical (laser) tweezers for manipulation. However, the optical fields that provide confinement and drive also result in electrodynamic interactions that are generally neglected. We address this issue with a detailed study of interparticle dynamics in an optical ring vortex trap using 150-nm diameter Ag nanoparticles. We term the resultant electrodynamically interacting nanoparticles a *driven optical matter system*. We also show that a superior trap is created by using a Au nanoplate mirror in a retroreflection geometry, which increases the electric field intensity, the optical drive force, and spatial confinement. Using nanoparticles versus micron sized colloids significantly reduces the surface hydrodynamic friction allowing us to access small values of optical topological charge and drive force. We quantify a further 50% reduction of hydrodynamic friction when the nanoparticles are driven over the Au nanoplate mirrors versus over a mildly electrostatically repulsive glass surface. Further, we demonstrate through experiments and electrodynamics–Langevin dynamics simulations that the optical drive force and the interparticle interactions are not constant around the ring for linearly polarized light, resulting in a strong position-dependent variation in the nanoparticle velocity. The nonuniformity in the optical drive force is also manifest as an increase in fluctuations of interparticle separation, or effective temperature, as the optical driving force is increased. Finally, we resolve an open issue in the literature on periodic modulation of interparticle separation with comparative measurements of driven 300-nm-diameter polystyrene beads that also clearly reveal the significance of electrodynamic forces and interactions in optically driven colloidal systems. Therefore, the modulations in the optical forces and electrodynamic interactions that we demonstrate should not be neglected for dielectric particles and might give rise to some structural and dynamic features that have previously been attributed exclusively to hydrodynamic interactions.

DOI: 10.1103/PhysRevE.95.022604

I. INTRODUCTION

There is much interest in understanding and controlling the collective motions that arise in driven systems of colloidal particles in solution [1–4]. These studies quantify of the influence of hydrodynamic interactions that also play a role in the collective dynamics of self-propelled active matter systems [5–8]. It is becoming increasingly common that optical fields and forces are used for these studies as intensity and phase gradients can confine particles without introducing physical boundaries that would alter the hydrodynamic interactions and yet can produce large deterministic forces to drive single polarizable microparticles or large numbers of them [1,9]. Shaped optical fields can be applied to manipulate single and multiple nanoparticles by optical forces arising from momentum transfer, e.g., trapping by intensity gradient forces exerted by a tightly focused Gaussian beam, or pushing by radiation pressure due to absorption and scattering [10,11].

Alternatively, light that possesses spin [12] or orbital angular momentum (OAM) [13] can cause nanoparticles to spin or undergo orbital rotational motion [14–17]. Optical beams possessing OAM are colloquially termed optical vortices [18], as these beams exhibit annular cross sections and tilted phase fronts. Following the observation of rotating microparticles driven by an optical vortex laser beam [19], the transfer of OAM from photons to microparticles has been widely exploited [14,18–32], especially for investigating hydrodynamic coupling between multiple particles [1,2,25,27,33–35].

In an optical vortex, each photon has an angular momentum of $l\hbar$, where l is the topological charge of the vortex (i.e., the total phase shift upon circling the vortex center divided by 2π) [13]. Theoretically, the angular velocity of a rotating particle will be linearly proportional to l assuming that the total photon flux incident on the particle is always the same [18,21]. However, this assumption is usually not valid. The classic optical vortices, i.e., Laguerre-Gauss beams [13], have varying radii depending on l [18], which means the intensity on the particle will change with different topological charges.

A vortex with constant intensity profile and radius that is independent of l is an ideal optical field to study motion and particle interactions as a function of the drive, or l. A class of "perfect optical vortices" (i.e., holographic ring traps) produced only using a spatial light modulator (SLM) was introduced in Roichman *et al.* [28] to study the dynamics of driven microparticles; a linear dependence of particle rotation rate on l was found only when $l \geqslant 20$ [9]. An alternative route to creating a "perfect optical vortex" [36] was recently

*Present address: Department of Chemical and Biomolecular Engineering, Clarkson Univeristy, Potsdam, NY 13699.

†Present address: Physics Department, Bar-Ilan University, Ramat Gan, 5290002 Israel.

‡nfschere@uchicago.edu

demonstrated by making an optical ring with an axicon and a lens and then adding OAM to the ring with a spatial light modulator (SLM) [37]. The dynamics of microparticles pushed against a coverslip surface by the optical vortex were investigated and a linear dependence of particle rotation rate on l was obtained, but only when $l \geqslant 2$; the particles did not start to rotate at $l = 1$ due to the frictional forces on the microparticles and the limited laser power [36]. Lehmuskero *et al.* [31] have recently demonstrated that (plasmonic) metal (Au) nanoparticles can be trapped and driven in focused optical vortex beams. Therefore, a better demonstration of OAM transfer could result from a tightly focused optical vortex and particles with smaller frictional forces, e.g., nanoparticles and/or trapping away from a surface.

Nonequilibrium studies of trapped and driven colloids such as those listed above focus on hydrodynamic forces. Yet, electrodynamic forces and interactions can be important [38–44]. The relative importance of hydrodynamic and electrodynamic interactions changes with particle size, particle spacing, and the constitutive nature of the particles (e.g., dielectric with small or large index of refraction or metallic particles, etc.). In fact, as the size of the particles decreases and with a suitable choice of material (e.g., metal) the intense scattering of the trapping field can lead to strong electrodynamic interactions amongst the particles [10,45–47].

In this article, we introduce and characterize a constant-radius optical vortex that is created by interfering a holographic ring trap using a retroreflection geometry with a gold (Au) nanoplate mirror [47]. We study the dynamics of single and multiple silver (Ag) nanoparticles driven by the optical vortex to clearly demonstrate OAM transfer from $l = -5$ to $l = 0$ to $l = +5$. We also perform comparative experiments with these nanoparticles trapped near an electrostatically slightly charged (repulsive) glass surface. We show that multiple nanoparticles in the optical vortex are electrodynamically coupled *via* optical binding interactions [14,38,46,47], resulting in the formation of optical matter [48], which is in distinct contrast with the hydrodynamically coupled microparticles in nearly all previous reports. The use of metal nanoparticles and the concomitant strong optical binding interactions are key aspects of our study. The experiments achieve modest nonequilibrium conditions, with Péclet numbers [3] in the range 0.2–5 for trapping at a glass interface or 3–75 when over a Au nanoplate mirror. Using combined electrodynamics–Langevin dynamics (ED-LD) simulations [49] we demonstrate that the optical drive force and the interparticle interactions vary in a sinusoidal manner for linearly polarized light, which is confirmed in experiment. The ED-LD simulations allow us to quantitatively explain how these electrodynamic interactions affect interparticle dynamics. We examine the dynamics of the electrodynamically interacting Ag nanoparticles in detail by varying the optical drive force in traps over glass and the Au nanoplate mirror demonstrating that the fluctuations or noise in the interparticle separations increase with increasing optical drive. Moreover, theory and model Langevin simulations allow explaining the increasing noise with increasing l, and hence the effective temperature of the interacting particle system as resulting from the periodic modulations in optical forces. Finally, we demonstrate, with comparative measurements of driven 0.3-μm-diameter polystyrene beads, that the electrodynamic interactions should not be neglected for driven dielectric particles, which might give rise to some structural and dynamic features that have been attributed exclusively to hydrodynamic interactions.

II. RESULTS AND DISCUSSION

A. Generating and characterizing an optical ring vortex

The optical ring vortex was produced by phase modulation of a linearly polarized Gaussian beam from a cw titanium sapphire laser operating at $\lambda = 800$ nm. The SLM modifies the incident Gaussian field with a phase function [28,50]

$$\phi(\vec{\rho}) = A J_l(C R \rho) e^{il\theta}, \tag{1}$$

where $\vec{\rho} = (\rho,\theta)$ denotes the polar coordinates relative to the optical axis, A is the amplitude of the incident Gaussian beam, J_l is the lth-order Bessel function of the first kind, C is a constant that is calculated from the focal length and wavelength of the optical system, and R is the radius of the ring (see Fig. 11 in the Appendix for images of the phase mask produced using the phase function above). In our case a microscope objective (Olympus 60x, $N.A. = 1.2$, SAPO) Fourier transforms the phase-modulated incident optical field and generates a focused optical ring vortex.

The three-dimensional (3D) profile of the optical vortex is illustrated in Fig. 1(a); the vortex evolves into an optical ring at the focal plane and its 3D intensity profile along the optical axis is symmetric across the optical ring. This symmetry

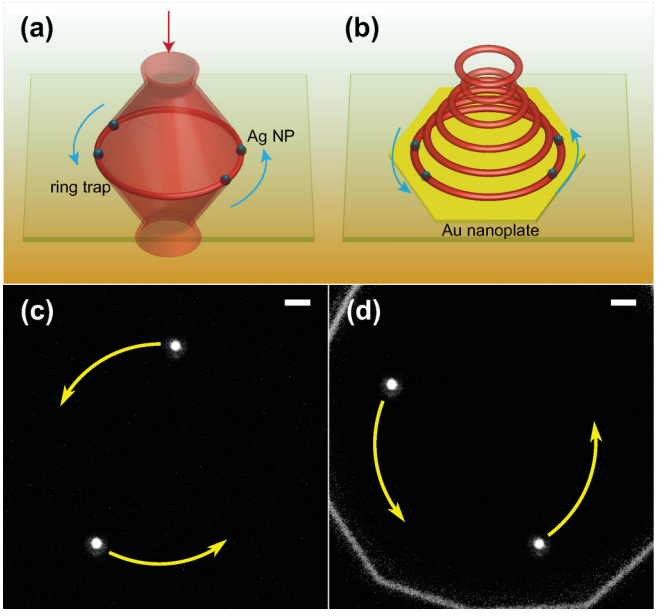

FIG. 1. Schematic of the focused optical beam and ring trap over (a) a glass coverslip and (b) a Au nanoplate. A dark-field optical microscope image of two Ag nanoparticles trapped (c) over glass and (d) over a Au nanoplate mirror. The bright line segments and polygonal shape are the edges of the Au nanoplate. Note the Au nanoplate overfills the panel. The curved arrows in (c) and (d) indicate the direction of rotation of the nanoparticles in the optical vortex ring trap. The white scale bars in (c) and (d) is 1 μm.

enables a retroreflection geometry when a Au nanoplate mirror is positioned at the focal plane, where the reflected beam interferes with the incident beam that generates a series of optical ring traps along the optical axis, as illustrated in Fig. 1(b). The optical ring trap we use in the experiments is the first fringe (antinode) of constructive interference above the Au nanoplate mirror, which is located approximately 250 nm away from the Au nanoplate surface. This particle center to nanoplate surface distance is determined from electrodynamics simulations (see Fig. 12). In the experimental configuration in Fig. 1(a) the scattering force pushes the particles towards the electrostatically charged glass surface but the Ag nanoparticles are also electrostatically charged with the same sign, so that the particles are repulsively trapped by the opposing scattering force of the optical trap and the electrostatic repulsion from the glass surface. In contrast, the surface-particle interactions and frictional drag are substantially reduced over the Au nanoplate mirror since the particles get trapped at the first interference fringe ~250 nm above the Au nanoplate surface. Therefore, the dynamics of the Ag nanoparticles are different in the two configurations.

The retroreflection and constructive interference also increases the intensity of the light in the trapping region by a factor of 4, resulting in a deeper trap potential that restricts the particles to a tighter ring than the analogous trap over the glass. Evidence of this is shown in the top two plots in Fig. 2(a) where the probability of finding a 150-nm-diameter Ag particle over glass (blue, left) has greater radial breadth (i.e., radial fluctuations) than for a nanoparticle over the Au nanoplate (red, right). The difference in the trap strength is more apparent when looking at the particle distributions in polar coordinates [Fig. 2(b)]. The radial width of the distribution of particle positions is larger when trapping over glass (blue, left) than over the Au nanoplate (red, right).

The difference between the nanoparticle trapping over glass or with the retroreflection over the Au nanoplate mirror can be approximately replicated in the simulation by using different electric field intensities. An electric field intensity I_0 is used in the ED-LD simulations over glass while the simulations over the Au nanoplate are performed with an intensity of $4I_0$ corresponding to a constructive interference antinode. Although the motion of the nanoparticles along the optical axis (z) would be different for trapping at the glass interface and over the Au nanoplate, we are interested in the motion of the particles driven in the transverse (x-y) plane of the optical axis. Therefore, the simple approximation of using twice the value of the incident field (or $4I_0$) is sufficient for the purpose of understanding the behavior for different drives. Figure 2(c) shows the trajectory of a simulated nanoparticle at intensity I_0 with an $l = 2$ applied angular force. The amount of radial diffusion qualitatively matches the distribution for the experiment over glass, shown in blue (left) in Figs. 2(a) and 2(b). The trajectory in Fig. 2(d), calculated from simulations with an intensity of $4I_0$ while keeping the same $l = 2$ angular force, matches the distribution of the particle positions in the experiment, shown in red (right) in Figs. 2(a) and 2(b). The total duration of the simulated trajectories shown in Figs. 2(c) and 2(d) are the same so it is clear from the figures that the particle moves a shorter distance for the lower intensity source. Movie S1 in the Supplemental Material [51] shows the simulated trajectories of particle for intensity I_0 and $4I_0$.

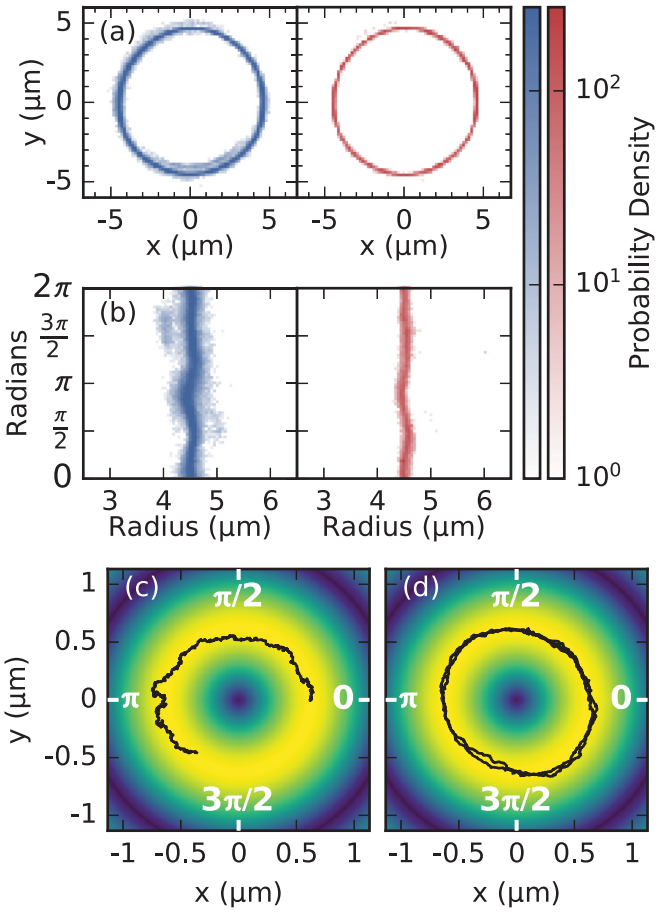

FIG. 2. Probability densities and simulated trajectories of particles in the ring traps. (a), (b) Probability densities of particles in the ring traps over glass (blue, left) or over plate (red, right). Distribution of the particle positions in (a) Cartesian coordinates and (b) polar coordinates in the laboratory frame. (c), (d) Electric field intensity (heat map) and particle trajectory from the simulation at intensity I_0 (c) and $4I_0$ (d) for $l = 2$. Example trajectories from the simulation are shown in black. (See Supplemental Material [51], movie S1.)

B. Imparting orbital angular force

Unlike traditional vortex beams, the intensity profile and the radius of the optical ring vortex are independent of l for the phase masks we apply (see Fig. 11), while the optical angular force in the optical trap can be varied as desired. The size and intensity of the optical ring vortex can be calculated by taking the Fourier transform of the phase mask for each l, showing that the trap's radius and intensity profile are independent of l (Fig. 11). However, the phase profile depends on l as seen in the third column of Fig. 11, where the phase gradient is $\nabla\phi = \frac{2\pi l}{2\pi R} = \frac{l}{R}$ around the ring. That phase gradient may be viewed as the source of optical angular force in the optical vortex. The phase gradient also gives rise to an optical force $F_l \propto I\nabla\phi$ [9,52] that will drive trapped particles around the ring. Since both intensity and radius are independent of l, it is easy to see that $F_l \propto l$, indicating that each increase in l results

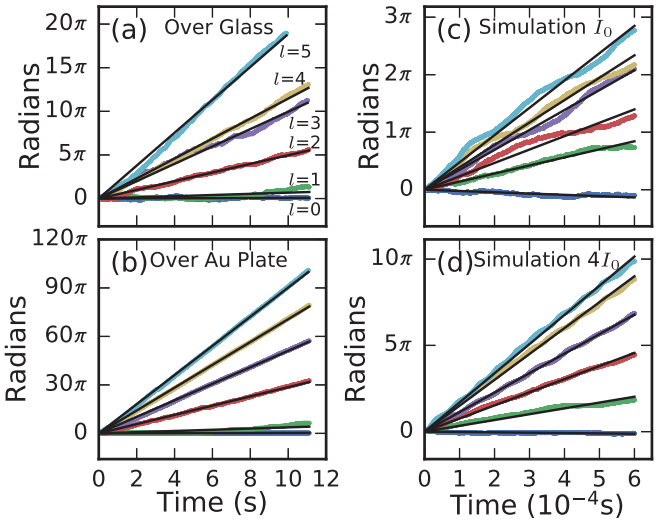

FIG. 3. Angular displacements vs time for experiments and simulations for glass and Au nanoplate conditions and angular drives $l = 0$–5. (a) Experimental trajectories of a single Ag nanoparticle rotation over glass (see Supplemental Material [51], movies S2–S4) and (b) over the Au nanoplate (See Supplemental Material [51], movie S5) for six different drives. (c) The trajectories of a single Ag nanoparticle rotation in the simulation with intensity at I_0 and (d) at intensity $4I_0$ for $l = 0$–5. The solid black lines are linear fits of the rotation (angular displacement) versus time.

in a linear increase of rotational force applied to the particles in the ring trap.

The angular optical force applied to particles is examined using the trajectories of Ag nanoparticles in an optical ring vortex. The position of a single Ag nanoparticle is recorded while l is increased every ∼11 s in a ring trap of $R = 9.5$ μm with l ranging from 0 to 5 both over glass and over a Au nanoplate. The same identical Ag nanoparticle is used for all measurements over glass and another for all measurements over the Au nanoplate mirror. The nanoparticle's trajectory is determined for each value of l over glass and over the Au nanoplate mirror. The $l = 0$ trajectories show only diffusive behavior of the nanoparticle both over glass and over the Au nanoplate [Figs. 3(a) and 3(b)]. However, when l is increased the nanoparticle makes deterministic orbits (but with fluctuations) around the ring. The trajectories show that a nanoparticle over the Au nanoplate [Fig. 3(a)] completes about six times as many rotations as a nanoparticle over glass [Fig. 3(b)] for a given l. In addition the trajectories have fewer fluctuations and more closely follow circular paths (i.e., straight lines in the polar representation) in experiments done over the Au nanoplate [Fig. 3(b)] than in the experiments over glass; the trajectories over glass are noisier around the linear fits [Fig. 3(a)]. Movies S2–S5 in the Supplemental Material [51] show the motion of the nanoparticles for $l = 0$, $l = 3$, and $l = 5$ over glass, and $l = 3$ over the Au nanoplate, respectively.

The trajectories calculated from simulations using intensities of I_0 and $4I_0$ show the same behavior as the experiments over glass and over the Au nanoplate, respectively. The trajectories from simulations of intensity I_0 [Fig. 3(c)] are noisier about the linear fit similar to those observed in the experiment over glass [Fig. 3(a)]. Likewise, the simulation trajectories at $4I_0$ [Fig. 3(d)] show a more linear increase in time just like the experimental results with the optical ring vortex over the Au nanoplate [Fig. 3(b)]. One difference between the simulated and the experimental trajectories is that there is a noticeable oscillatory deviation from a straight line of the trajectory seen in the simulations, especially for $l = 4$ and $l = 5$ in Figs. 3(c) and 3(d). The oscillatory deviation will be addressed below.

It should be noted that the simulated optical ring vortex is not the same size as in the experiments mainly due to restrictions on available computational resources and memory. As a result of the smaller size (diameter) of the simulated ring trap and to facilitate more angular motion (rotations) in the ∼2-ms-long simulated trajectories, the electric field intensity is 30 times larger than in the experiments. The main consequence of the smaller ring size and larger electric field intensity is that the optical forces and therefore the particle velocities are larger. However, as seen from Fig. 3 and the figures below, the qualitative agreement between the experimental and the simulation data is striking.

The mean squared displacement (MSD) of single particle trajectories reveals the strength of the drive force for different values of l. The MSD from experiment and simulation [Figs. 4(a)–4(d)] can be fit with

$$\mathrm{MSD}(\tau,l) = 2D(l)\tau + \frac{F(l)^2}{\gamma^2}\tau^2, \tag{2}$$

where $D(l)$ is the l-dependent diffusion constant [53,54], $F(l)$ is the optical force, γ is the friction coefficient, and τ is the lag time. Here, we assume that the diffusion constant is independent of the angular drive. The diffusive character of the trapped nanoparticle is most apparent over the glass surface [Fig. 4(a)] for short time scales demonstrated by the curve when τ <0.1 s where the linear term in the MSD is dominant, while when τ >0.1 s the squared term dominates and the particle's motion is determined primarily by the optical force. Nanoparticles trapped over the Au nanoplate exhibit much less transverse diffusive behavior; the motion of the particles is dominated by the optical drive force [Fig. 4(b)].

The plot of $F(l)/\gamma$ as a function of l in Fig. 4(e) using the fitting parameters from Figs. 4(a)–4(d) shows that the optical force increases linearly with l from −5 to 5. This result, which is consistent with the theoretical analysis, clearly demonstrates that the optical angular force transfer is linearly proportional to l. Moreover, the slope of $F(l)/\gamma$ over the nanoplate is 5.5 times that over the glass. Constructive interference over the Au nanoplate only increases the intensity of the trap by fourfold and the angular force $F(l) \propto I$, intensity, so the additional increase of the slope indicates that the friction coefficient γ decreases over the nanoplate. The effect of the hydrodynamic friction is apparent when comparing the simulation results in Fig. 4(e) to the experimental ones. When the simulation for intensity $4I_0$ [Fig. 4(e), open circles] is aligned with the experimental results over the nanoplate mirror [Fig. 4(e), closed circles] the corresponding simulation results for intensity I_0 [Fig. 4(e), open triangles] do not align perfectly with (i.e., have a different slope than) the experimental results obtained over the glass [Fig. 4(e), closed triangles]. The

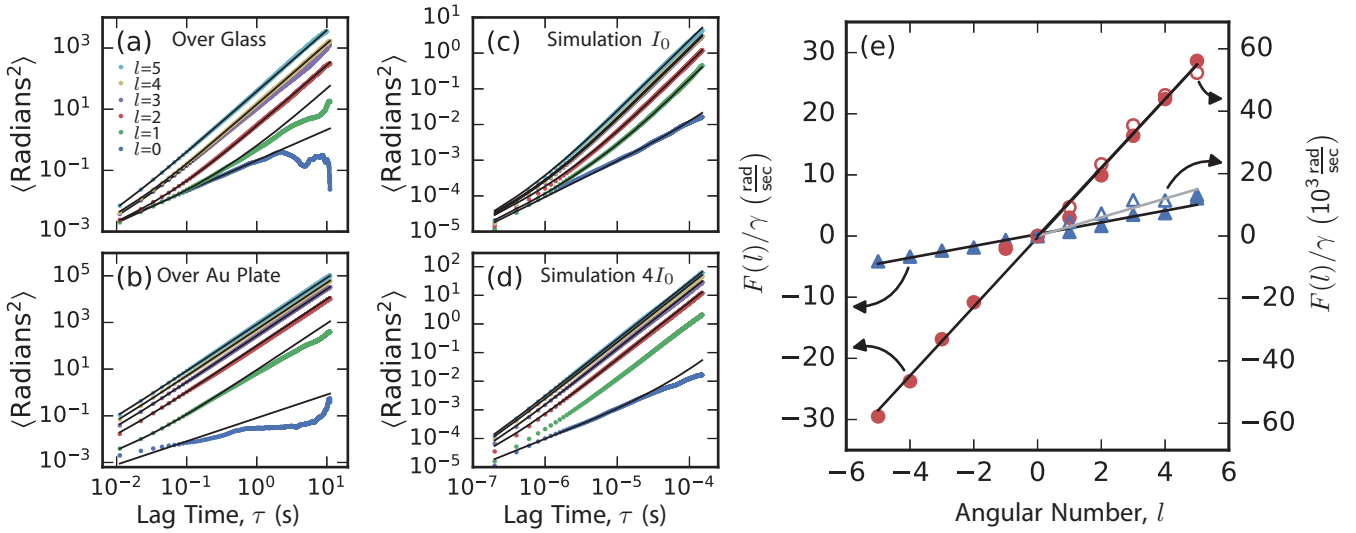

FIG. 4. MSD of experimental and simulated particle motion and forces on Ag nanoparticles from experiment and simulation. (a), (b) Angular MSD for different angular drives l from the experiment trapping over the glass surface (a) or over the nanoplate mirror (b). (c), (d) Angular MSD for different angular drives l from simulations with intensity I_0 (c) and $4I_0$ (d). The MSDs for (a)–(d) are calculated from the angular displacement vs time results from Fig 3. (e) Fit parameters of $F(l)/\gamma$ from the MSD of single nanoparticles in the optical ring vortex over glass (closed blue triangles) and over the Au nanoplate (closed red circles) using the left y axis. Fit parameters of $F(l)/\gamma$ from the MSD of single nanoparticle simulations for I_0 (open blue triangles) and $4I_0$ (open red circles) using the right y axis. Solid black lines show linear fits to the data, the solid gray line shows the fit to $F(l)/\gamma$ vs l for intensity I_0 in the simulation. Note that the vertical axes are chosen so that the fitted lines to the Au nanoplate (and $4I_0$) results are identical.

90–100-nm separation of the nanoparticle surface from the glass surface, estimated from a Derjaguin-Landau-Verwey-Overbeek (DLVO) potential treatment for the electrostatics measured and estimated for the experiment (see Appendix D), is within the distance where hydrodynamic interactions with the surface are significant [55,56]. Therefore, we believe that the discrepancy between the slopes shows the effect of the hydrodynamic friction present in the experiments over glass, which is not accounted for in the simulation.

The oscillating deviations from a linear fit to the particle trajectories found in the simulation [shown in Figs. 3(c) and 3(d)] reflect periodic modulations of the particle's velocity. The particle speed is plotted as a function of its position on the ring in Figs. 5(a) and 5(b). The speeds are calculated using single particle trajectories; both the experimental and the simulation results show a large change of the instantaneous speed as a function of the angular position around the ring. Both the experiment and the simulation show similar angle-dependent modulation of the speed, that behaves as a sine function centered around a nonzero mean value. Figures 5(c) and 5(d) show vector maps of the optical forces acting on a 150-nm Ag particle for $l = 0$ and $l = 4$, respectively. The

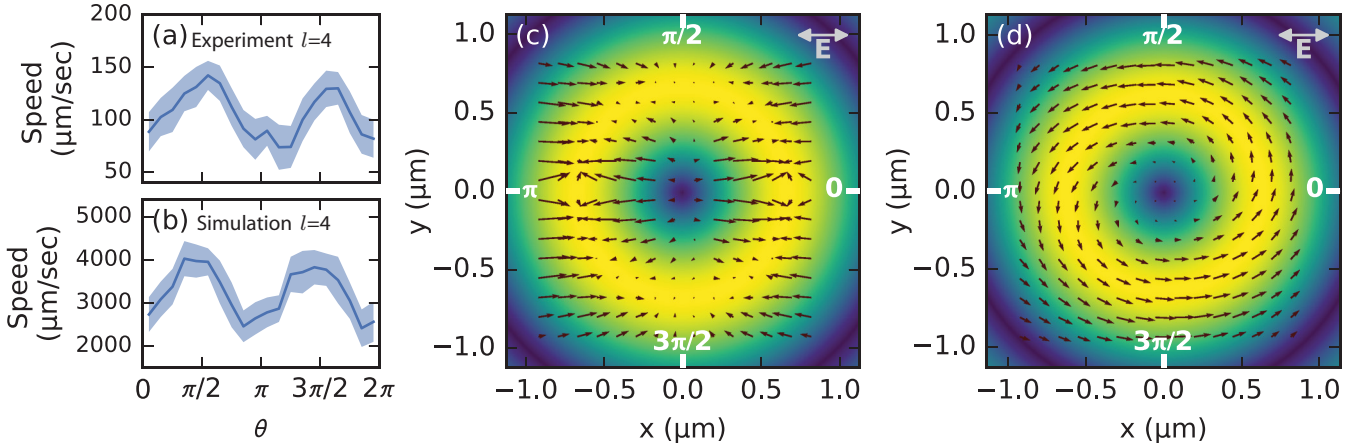

FIG. 5. Speed and force information of nanoparticles in the optical ring vortex. (a), (b) Speed as a function of position around the optical ring vortex in (a) the experiment over the nanoplate mirror at $l = 4$ and (b) in the simulation at intensity $4I_0$ at $l = 4$. The speeds are calculated by taking the difference between the Cartesian positions of the nanoparticles in successive frames in the experiment or time steps in the simulation and dividing by the time increment (e.g., 1/frame rate). (c), (d) Electric field intensity (heat map) and force vector map in the $4I_0$ simulation at $l = 0$ (c) and $l = 4$ (d).

direction of polarization (horizontal) is indicated by the gray arrow in the top right corner. The optical forces are calculated from the Maxwell stress tensor by placing the Ag nanoparticle at each position and performing an finite-difference time-domain (FDTD) simulation to determine the total fields. Larger magnitude optical force vectors are seen in the 0 and π regions of the optical ring vortex for $l = 0$ and in the $\pi/2$ and $3\pi/2$ regions for $l = 4$, respectively. This makes it clear that the linear polarization of the beam creates an anisotropy in the optical forces and results in the velocity oscillations revealed in Figs. 5(a) and 5(b). The force anisotropy for linearly polarized vortex beams was also noted by Lehmuskero *et al.* [31]. The anisotropy or modulation in the optical forces for linearly polarized light has important consequences for the dynamics of the nanoparticles driven in the optical ring vortex as discussed below.

C. Electrodynamic interparticle interactions

As previously shown [46,47,57], Ag nanoparticles interact electrodynamically *via* optical binding; a periodic modulation of the electric field in the vicinity of the nanoparticle resulting from interference of the incident field and the scattered field from each particle. The strength and spatial aspects of optical binding depend on the polarization of the incident beam [46]. In the present experiment the polarization of light is held constant; it is horizontally polarized in the reference frame of the rings shown in the figures. This produces particle-particle interactions that depend on the location of the particles as they move in the ring trap. Pairs of nanoparticles oriented perpendicular to the light polarization direction have a stronger optical binding interaction than do pairs of nanoparticles aligned parallel [46]. A peak in the probability distribution of interparticle separations at the nearest-neighbor distance results from an optical binding interaction.

The distribution of the nearest-neighbor separations shown in Fig. 6 demonstrates the effect of polarization on interparticle interactions as a function of angle in the optical ring vortex. These interparticle separations can be further grouped based on sections of the ring trap where particles can arrange aligned parallel to or perpendicular to the polarization. The dashed lines in Fig. 6 indicate the sections of the optical ring vortex that are binned for the different configurations relative to the polarization of light. Particle pairs are considered parallel to the polarization if they are in a $\pi/8$ slice of the ring centered on the $\pi/2$ or $3\pi/2$ positions. Likewise, particle pairs are perpendicular to the polarization if they are in a $\pi/8$ slice of the ring centered on the 0 or π positions. Figure 6 demonstrates that the particles prefer optical binding separations when in the 0 and π positions; the distributions show increased probability to be separated by 0.6, 1.2, and 1.8 μm, which is consistent with past experimental and theoretical results for optical binding [46]. The positions at $\pi/2$ and $3\pi/2$ in Fig. 6 do not show the same effect because the optical binding interactions are weaker for particles aligned parallel to the polarization.

D. Distributions of interparticle separations

The nearest-neighbor separations are examined in the regions where the polarization is aligned parallel or perpendicular to the particles in the ring trap with respect to the driving force for the over-glass vs over-nanoplate conditions. Experiments over glass shown in Figs. 7(a)–7(c) demonstrate that the optical binding interactions are much more pronounced for nearest neighbors perpendicular to the polarization than particles parallel to the polarization. The emergence of particle interactions at separations corresponding to the second optical binding distance (site) at 1.2 μm are also noticeable, but only observed for particles aligned perpendicular to the polarization where the binding is stronger. The optical binding increases dramatically over the Au nanoplate as seen in Figs. 7(d)–7(f) because the particles trapped in the antinode created by retroreflection experience a fourfold increase in intensity. Here, the first, second, third, and perhaps the fourth optical binding sites are evident.

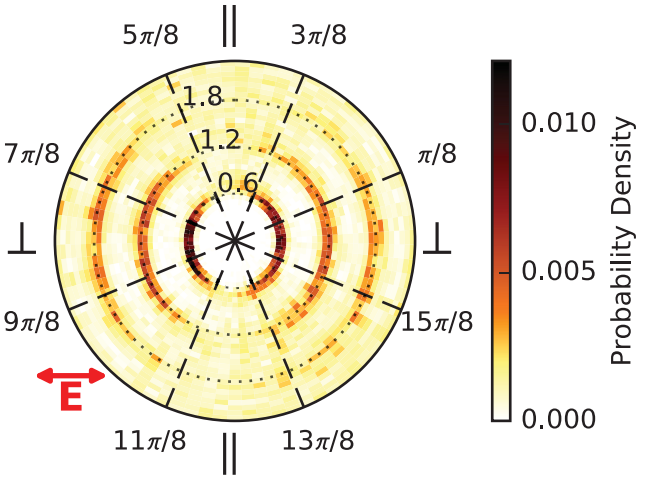

FIG. 6. Probability density plot of interparticle separations characterized as parallel or perpendicular with respect to the electric field polarization (horizontal to the ring trap). The interparticle separation is plotted with respect to the angular location of the midpoint of a pair. The radial coordinate is the interparticle separation (in μm units). The color represents the probability density of events in the radial and angular coordinates. Four of the octants of the ring trap are categorized as parallel or perpendicular with respect to the electric field. These octants, labeled $\perp$ and $\parallel$, are sections of the optical ring vortex where the trap is perpendicular or parallel to the electric field polarization. This data is from a multiparticle experiment at $l = 2$ over glass. Similar results are obtained for other values of l and also over the Au nanoplate.

The distributions of interparticle separations can be further classified based on the magnitude of the optical angular drive force $F(l)$ applied in each experiment. We observe that the noise (fluctuations) increase with increasing optical drive force and that this competes with the attractive optical binding interactions. Figure 7(a) shows that the optical binding interactions dominate in the probability distributions of the interparticle separation for small l ($l = 0$, 1, 2), where the first binding site at 0.6 μm is strongly populated and the emergence of the second binding site can be seen at 1.2 μm for particles over glass. Likewise, Fig. 7(d) shows that very narrow distributions at the first, second, third, and fourth binding distances arise over the Au nanoplate mirror. As the optical drive force increases the distributions broaden around each

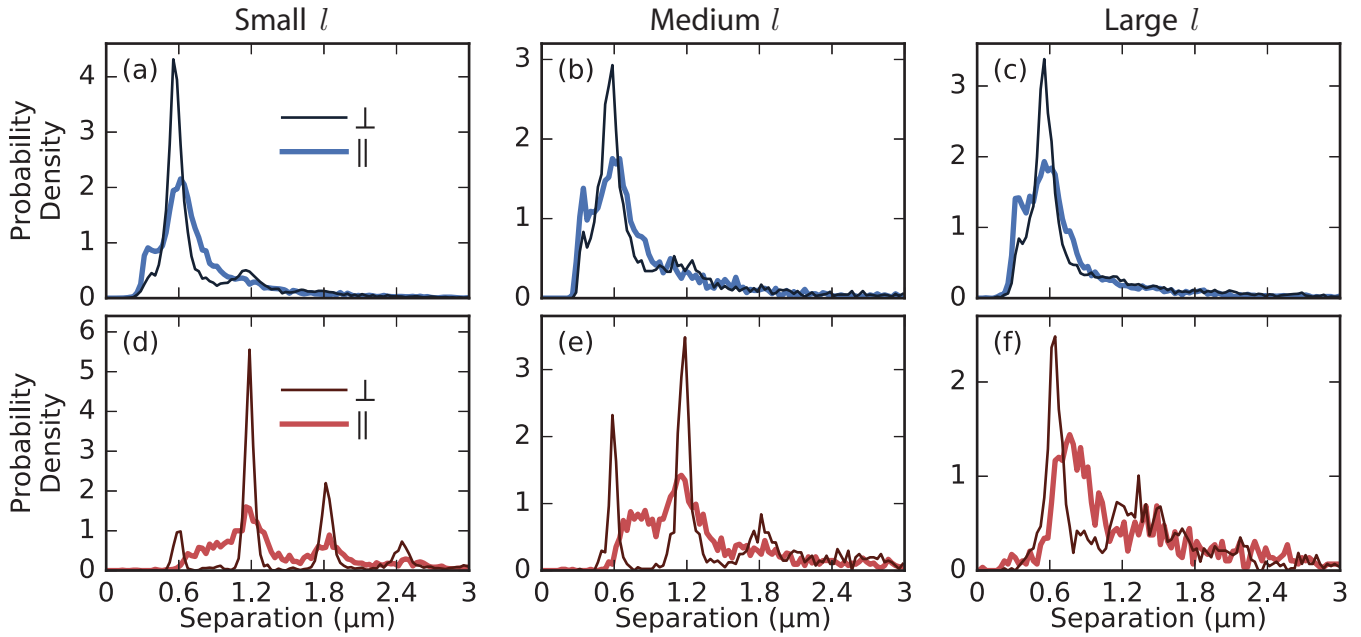

FIG. 7. Conditional probability distributions of the nearest neighbor separation grouped into categories of (a), (d) small ($l = 0$–2), (b), (e) medium ($l = 3$), and (c), (f) large ($l = 4$–5) applied optical force for experiments over glass (blue, top row) and over the Au nanoplate (red, bottom row). In each panel there are distributions for particle pairs that are parallel (thick light colored curve) or perpendicular (thin dark colored curve) to the polarization. The separations are binned parallel or perpendicular based on the scheme in Fig. 6. Curves are plotted through the midpoints of the distribution bins.

optical binding site [Figs. 7(b) and 7(e)]. Finally, at large l ($l = 4$, 5), the distributions are so broad that evidence for optical binding interactions largely disappears beyond the first site at 0.6 μm [Figs. 7(c) and 7(f)].

We also examined the dynamics of interparticle separations by performing ED-LD simulations with two 150-nm Ag nanoparticles in the optical ring vortex. Unless specified, the two particles were initialized with a separation of 0.6 μm, corresponding to the first optical binding separation, and placed symmetrically around the 0° position in the ring. Figure 8(a) shows the probability densities of the interparticle separations for different values of l. For small l (i.e., $l = 0$–1) we obtain a strong peak in the probability density around the first optical binding location (0.6 μm). Increasing the optical driving force on the particles leads to broadening of the first peak and the emergence of probability density at the second (for medium l, i.e., $l = 2$–3) and third (for large l, i.e., $l = 4$–5) optical binding separations. Thus, the particles separate more easily from their initial condition at the first optical binding site with increasing l. These simulation results are consistent with the experimental results of Fig. 7. We determined the potentials of mean force at the first optical binding site from the interparticle probability densities for the different values of l. As shown in Fig. 8(b), these results demonstrate a diminishment of the effective optical binding potential with increasing l. This means that the noise of the system increases with drive. Further, as shown in Figs. 8(c) and 8(d), we determined the probability densities and corresponding potentials of mean force at the location of the first optical binding site with no optical drive (i.e., $l = 0$) in the regions where the polarization of the incident field is aligned perpendicular and parallel to the interparticle axis. Together with the experiments (Fig. 7), these results demonstrate that optical binding is weaker when the polarization is parallel to

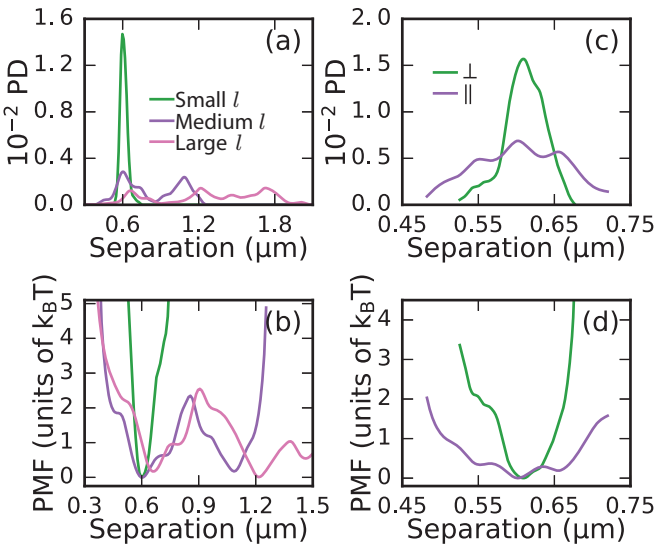

FIG. 8. Simulations of two Ag nanoparticles in an optical ring vortex with electric field intensity $4I_0$. (a) Probability density (PD) distributions of nearest neighbor separations for nanoparticle pairs in the simulation for $l = 0$–1 (small l), $l = 2$–3 (medium l), and $l = 4$–5 (large l). (b) Potentials of mean force (PMF) around the first two optical binding sites calculated from the probability densities from (a). (c) Distributions of interparticle separations calculated from simulations for $l = 0$, where the two particles are initialized symmetrically about the $\perp$ (0) or the $\parallel$ ($\pi/2$) positions in the ring. (d) Potentials of mean force for $l = 0$ at $\perp$ (green) and $\parallel$ (purple) calculated from the probability densities in (c). All curves are plotted using a Gaussian kernel density estimator.

the interparticle axis, leading to a broader distribution in the probability density that reflects a shallower (weaker) effective potential.

E. Increasing effective temperature with drive force

The experimental and simulation results in Figs. 7 and 8 show that increasing the optical drive force causes an increase in the effective temperature of the system; a larger optical drive force causes particles to fluctuate more and with greater magnitude about the optical binding sites. Note that the total optical intensity on the particles is constant so particle heating is constant for all values of l. The increase in the fluctuations, and therefore the effective temperature with increasing l, could result from the modulation in the optical binding potential. We used the following minimal model system to test this hypothesis. Imagine two particles confined to the perimeter of a circle (as in the experiments) with an angular modulation of the interparticle potential. Assuming over-damped dynamics, we show in the Supplemental Material [51] that the effective potential of mean force between the two particles, in the limit that the driving force is large, is simply the potential of mean force of the undriven system averaged over the entire ring. In other words, in the high drive limit the effective potential is the average of the modulated potential [58] and thus the driving force reduces the well depths and barriers in the modulated potential. Therefore, the variance of the probability distributions of the particles is determined by an effective force constant $k_{\text{eff}} = (k_{\text{min}} + k_{\text{max}})/2$ where k_{min} and k_{max} are the minimum and maximum force constants of the modulated (assumed) harmonic interparticle potential.

However, Fig. 5 indicates that the optical drive force that any particle in the ring vortex experiences is also modulated for linearly polarized incident light. The modulation in the optical drive force comes from asymmetry in the optical gradient while the optical binding interactions (Figs. 7 and 8) are altered by their orientation with respect to the direction of linear polarization. The effects of both kinds of force modulations, i.e., modulation in optical binding and optical driving force, are combined in the probability densities obtained from experiments and the ED-LD simulations and therefore cannot be used to identify the dominant mechanism that leads to the increase in fluctuations (i.e., increase in the effective temperature).

In order to separate the effects of the modulated optical binding and the modulated optical drive forces, we perform 1D Langevin dynamics (LD) simulations with periodic boundary conditions and impose a sinusoidal variation in the modulation of both the binding and drive forces. We assume a harmonic potential for optical binding and use the maximum and minimum force constants from the full ED-LD simulations for $l = 0$ shown in Fig. 8(d). Optical binding forces result from the interactions of the incident and the scattered fields and depend on the wavelength and intensity of the beam, and size of the particles. The size and intensity of the optical ring vortex does not depend on the value of l, therefore, optical binding forces can be assumed to be independent of l. The optical drive forces for different l are extracted from full ED-LD simulations of a single nanoparticle in the trap. The 1D Langevin equation, the optical drive force F_{d}, and optical binding force F_{b} for the ith particle in these simulations are

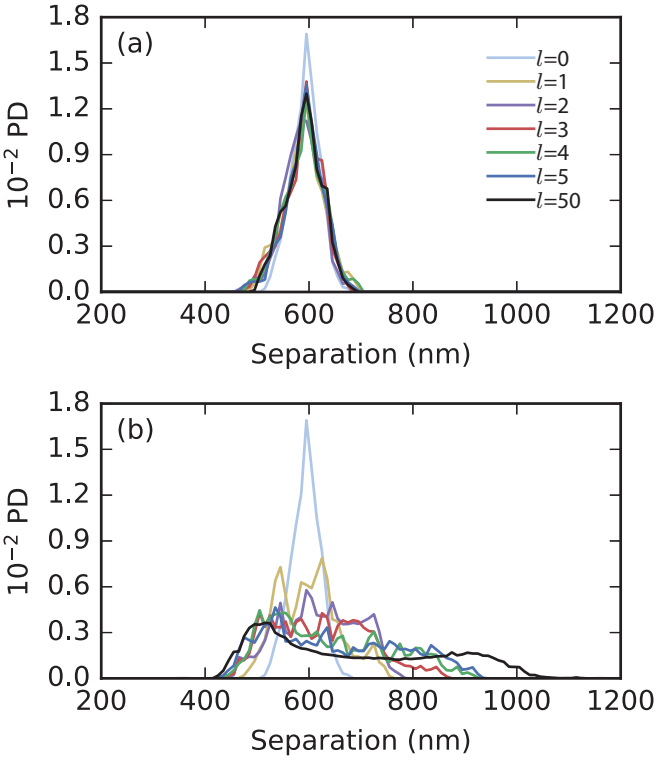

FIG. 9. Interparticle separation probability density (PD) functions affected by periodic modulation of (a) interparticle potential or (b) drive force. 1D LD simulations with periodic boundaries of two particles using parameters extracted from the full ED-LD simulations assuming (a) constant drive and modulated interparticle potential and (b) modulated drive and interparticle potential. (See Fig. 14 and Supplemental Material [51] movie S6.)

$$m\frac{d^2\theta_i}{dt^2} = F_{\text{d}}(\theta_i) + F_{\text{b}}(\theta_i) - \lambda\frac{d\theta_i}{dt} + \eta, \tag{3}$$

where θ_i is the position of the ith particle, λ is the Stokes drag friction coefficient, η is the stochastic thermal noise. The optical forces are:

$$F_{\text{d}}(\theta_i) = (F_{\text{max}} - F_{\text{min}})\sin^2(\theta_i) + F_{\text{min}}, \tag{4a}$$

$$F_{\text{min}} = l(1.5 \times 10^{-12}\ \text{N}), \tag{4b}$$

$$F_{\text{max}} = 2F_{\text{min}}, \tag{4c}$$

$$F_{\text{b}}(\theta_i) = -\frac{d}{d\theta_i}U_{\text{b}}(\theta_i), \tag{4d}$$

$$U_{\text{b}}(\theta_i) = k(\theta_c)(\theta_i - \theta_j - \theta_{\text{b}})^2, \tag{4e}$$

$$k(\theta_c) = (k_{\text{max}} - k_{\text{min}})\cos^2(\theta_c) + k_{\text{min}}, \tag{4f}$$

where $k_{\text{max}} = 3 \times 10^{-6}$ N/m and $k_{\text{min}} = 0.25k_{\text{max}}$ are the force constants, $\theta_c = (\theta_i + \theta_j)/2$ is the center of mass position of the two particle system, and θ_{b} is the separation corresponding to the first optical binding site (0.6 μm).

We perform the 1D LD simulations with two nanoparticles by assuming a modulated optical binding force but keeping a constant optical drive force, and by modulating both the binding and driving forces. The results are shown in Figs 9(a)

and 9(b), respectively. In the simulations with a constant driving force but modulated binding forces, we find that the effective force constant obtained from the probability distributions is the average of the maximum (at locations of 0 and π) and minimum (at locations of $\pi/2$ and $3\pi/2$) force constants for larger driving forces. However, the probability densities do not change appreciably with increasing l for the values of force constants ($k_{\max}$, $k_{\min}$) extracted from our ED-LD simulations. On the other hand, by including a modulating driving force in the 1D LD simulations, we find that the probability densities broaden with increasing l and a two-peaked distribution emerges for very large drive ($l = 50$). This result is reminiscent of the changes in the probability densities and potentials of mean force of Fig. 8. We illustrate the drive-force-induced modulation in Fig. 14 and Supplemental Material [51] movie S6. Movie S6 shows that the interparticle separations are modulated more strongly at large l for a modulated optical drive force, illustrating the origin of the increasing breadth of the probability density function of Fig. 9(b). These LD simulations combined with the analytical theory explain that the rise in effective temperature of the system with increasing l stems from the modulation in the optical driving force that is inherent to the linearly polarized beam.

The increase in the interparticle fluctuations and single particle dynamics due to the modulated drive force is reminiscent of the topic of enhanced or giant diffusion [59–63]. However, our study concerns force modulation as opposed to constant drive over a periodically modulated potential as proposed by Hänggi and co-workers [64]. Therefore, although the isomorphism may seem clear, we foresee subtleties that will be addressed in a separate publication.

F. Optical binding in driven dielectric colloids

We also considered whether electrodynamic interactions (i.e., optical binding) are significant for dielectric (polystyrene) particles trapped using the same optical ring vortex. The large peak in the probability density at a separation of 0.6 μm for the 300 nm polystyrene particles in Fig. 10(a) and another peak at a separation of 1.2 μm corresponding to the second optical binding site for particles oriented perpendicular to the polarization is a strong indication of optical binding. The inset in Fig. 10(a) shows the difference of the perpendicular and parallel distributions of the nearest neighbor separations, which exhibits characteristics of optical binding seen in Ag nanoparticles over glass [Fig. 10(b)] such as a broader and smaller amplitude parallel peak and the emergence of the optical binding at 1.2 μm.

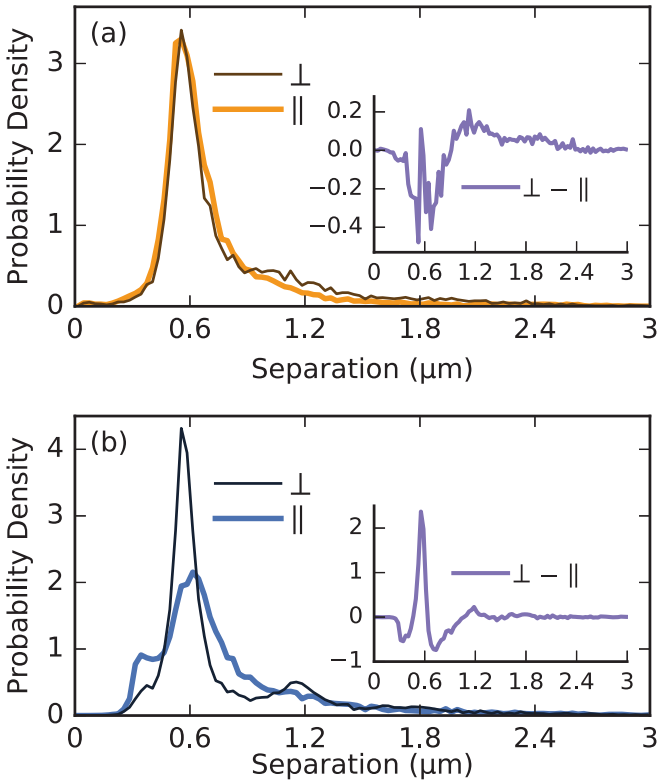

FIG. 10. Distributions of nearest neighbor separations. (a), (b) Probability densities of interparticle separation for (a) 300-nm polystyrene particles in the optical ring vortex over glass at $l = 1$ for both parallel and perpendicular positions in the ring and (b) Ag nanoparticles over glass for small l [same as Fig. 7(a)]. The insets for (a) and (b) show the difference (perpendicular minus parallel) of the respective distributions.

III. CONCLUSIONS

We have examined the properties of driven optical matter composed of metal nanoparticles in a optical ring vortex. The creation of a superior optical ring vortex by retroreflection from a Au nanoplate mirror is a technical advance that allows trapping particles in an interference antinode above the Au surface. The interferometric trap improves the axial tightness of the trap while also increasing the optical force on the nanoparticles and has reduced hydrodynamic friction as compared with particles that are moving in a vortex trap near a glass surface. Using 150-nm Ag nanoparticles in the optical ring vortex, we demonstrated in experiment and simulation that the optical drive force around the ring vortex trap is inherently modulated for a linearly polarized beam. This modulated force affects the interparticle interactions so as to increase the noise (or effective temperature) and effectively weaken the long-range attractive optical binding interactions.

We developed a model system and simulations showing that the increase in effective temperature (or fluctuations in interparticle separations) results mainly from the modulation in the optical drive force associated with the linear polarization of the incident beam. These electrodynamic forces and interactions in optically driven systems are often not considered in studies of hydrodynamically interacting driven colloidal systems. While the optical binding interactions may not dominate the interactions between larger dielectric particles, we want to encourage the understanding of their existence in these types of driven optical systems. Moreover, the modulation in the electrodynamic driving force that is inherent in a linearly polarized optical ring vortex will affect the interactions between colloidal particles currently ascribed to be solely due to hydrodynamic interactions [2] and is the dominant cause of persistent oscillatory dynamics of optically driven systems [4]. Finally, the modulation of the optical drive

force that we study here and the significant increase in noise with drive force that we find in experiment and explain via simulations and theory bears strong resemblance to the topic of "enhanced diffusion" [59–63]. We plan to address this topic in detail in a separate publication.

ACKNOWLEDGMENTS

We thank C. Peterson for thoughtful discussions. The authors would like to acknowledge support from the Vannevar Bush Faculty Fellowship program sponsored by the Basic Research Office of the Assistant Secretary of Defense for Research and Engineering and funded by the Office of Naval Research through Grant No. N00014-16-1-2502. The simulations were performed at the Center for Nanoscale Materials, a U.S. Department of Energy Office of Science User Facility under Contract No. DE-AC02-06CH11357. We also acknowledge the University of Chicago National Science Foundation Materials Research and Engineering Center for partial support.

P.F. and N.S. contributed equally to this work.

APPENDIX A: METHODS

1. Experiment

The experiments were performed using dark field microscopy with optical tweezers. Sample cells were mounted on an inverted microscope (Olympus IX71) and imaged through a 60× water immersion objective (Olympus UPLSAPO). Magnification was further increased with both 2× and 1.6× expansion lenses. The optical tweezer was created using a linearly polarized Gaussian beam ($\lambda = 800$ nm) from a Ti:sapphire laser that is shaped by a spatial light modulator (Hamamatsu X10468-02) to generate vortex ring traps of varying azimuthal phase gradients. Images of the trapped nanoparticles were recorded with an array detector (Andor Neo sCMOS DC-152Q-C00-F1) at a frame rate of 90 frames/sec with an exposure of 0.4 ms.

Sample cells were created by sandwiching a 180-silicone rubber spacer between two coverslips. A solution of Au nanoplates are drop cast onto the coverslip inside a cutout of the spacer. A diluted solution of spherical Ag nanoparticles (150 ± 9.6 nm diameter, nanoComposix) is placed inside the cut out of the spacer and another coverslip is placed over it creating a sealed sample cell. The sample cell is oriented such that the coverslip with the Au nanoplates is on top and the objective images through the bottom coverslip. This allows the laser to push particles to the top surface by the scattering force where particles can be trapped near the top surface over glass or a nanoplate mirror. However, due to electrostatic repulsion between the particles and the glass the particles do not touch the glass (or Au surface) and instead are repulsively trapped by the opposing scattering and electrostatic forces. A phase gradient encoded in the spatial light modulator controls the angular force applied to the particles in the ring trap.

The nanoparticle positions and trajectories are extracted from the images using the Mosaic Suite ImageJ plugin [65]. A kernel radius of 6 pixels with a 0.05 percentile threshold for the brightest maxima is used for particle localization. A large max displacement of 150 pixels between frames was used for linking particle positions into trajectories. Particle trajectories were checked manually to make sure the particle positions were properly linked between frames.

2. Numerical

Simulations of one and two Ag nanoparticles in an optical ring vortex trap were performed using a coupled electrodynamics–Langevin dynamics (ED-LD) solver that we developed [49]. The ED-LD simulation self-consistently couples the finite-difference time-domain (FDTD) method of solving Maxwell's equations with a splitting-method scheme for integrating the Langevin equation. The optical ring vortex beam is introduced in the simulation using the scattered field technique [66,67] in which the incident electric field is described in cylindrical coordinates as

$$\vec{E}(\rho,\theta,z) = \hat{x}\, E_0 J_l(kC_\rho \rho) e^{il\theta} e^{i(kz-\omega t)}. \tag{A1}$$

Here, $E_0 = \sqrt{2I_0/n\epsilon_0 c}$ is the electric field magnitude and I_0 is the intensity of the beam, l is the number of 0 to 2π angular phase rotations around the ring, J_l is a Bessel function of the first kind of order l. We use the constant C_ρ as an adjustable parameter that is varied in order to keep a constant radius for the beam. The incident magnetic field is calculated from Ampere's law for each time step before updating the scattered fields in the main FDTD calculation. The electrodynamic forces on the Ag nanoparticles are calculated using the Maxwell stress tensor, while the electrostatic forces due to surface charges are calculated using Coulomb's law. The Drude model is used to describe the dispersive Ag nanoparticles using the auxiliary differential equation method [67]. We use the following Drude parameters for Ag: $\epsilon_\infty = 3.045$, $\omega_p = 2.117 \times 10^{15}$ s^{-1}, and $\gamma_p = 6.069 \times 10^{13}$ s^{-1}. The total force (electrodynamic + electrostatic) on each nanoparticle is used in the Langevin equation to calculate the nanoparticle trajectories. Since we are interested in the driven (transverse) motion of the nanoparticles, we only use the transverse forces to simulate their trajectories. We were able to simulate a maximum of ∼2-ms-long trajectories with the computing resources available to us. Therefore, in order to generate multiple particle orbits around the ring, we simulate a smaller (∼2 μm) diameter optical ring vortex with an electric field intensity that is roughly 30 times that in the experiments. The details of the coupled ED-LD simulation can be found in Sule *et al.* [49]

APPENDIX B: OPTICAL RING VORTEX

Please see Fig. 11 for the phase masks on the SLM and a schematic of the optical ring vortex.

APPENDIX C: ELECTRIC FIELD OVER THE AU NANOPLATE

We estimate the electric field over the Au naoplate from the FDTD simulations. Figure 12 shows the electric field intensity in the retroflection geometry over the Au nanoplate mirror discussed in the main text. The electric field intensity is largest 250 nm away from the Au nanoplate surface where the Ag nanoparticles are trapped.

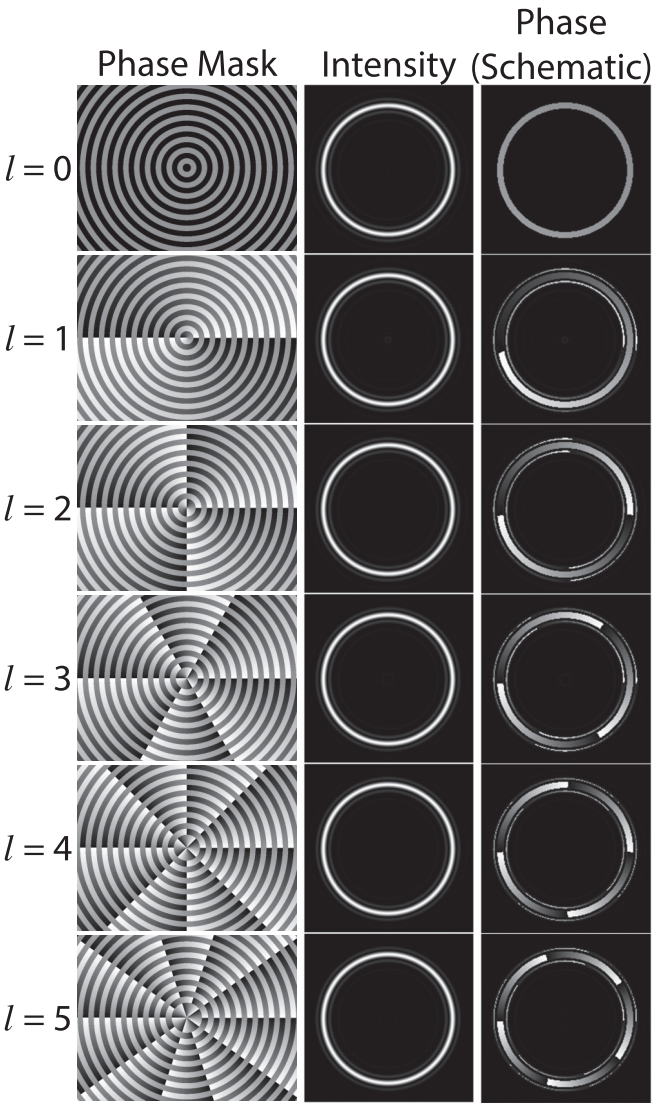

FIG. 11. Diagram showing the properties of the optical ring vortex for different l's. The first column shows the phase mask used on the SLM to produce the ring trap. The second column shows the intensity of the beam for each l, which is the same for all l's. The third column shows a schematic of the phase of the optical ring vortex for each l.

APPENDIX D: SEPARATION OF Ag NANOPARTICLE AND GLASS SURFACE

1. Electrostatic contribution

a. DLVO theory

DLVO theory uses the idea that the electrostatic interactions are a combination of two competing forces, the van der Waals attractive force and the double layer repulsive forces [68]. These potentials describe all of the electrostatic forces, the glass surface, and a Ag nanoparticle (in the absence of the optical trapping beam) as a function of their separation d,

$$W(d) = W_{\mathrm{A}}(d) + W_{\mathrm{R}}(d). \tag{D1}$$

Here, $W_{\mathrm{A}}(d)$ is the potential energy from the attractive van der Waals interaction, $W_{\mathrm{R}}(d)$ is the potential energy from repulsive electrostatic interactions, and $W(d)$ is the total potential energy. The Ag nanoparticle interacting with the glass is treated as a spherical particle interacting with an infinitely flat plate.

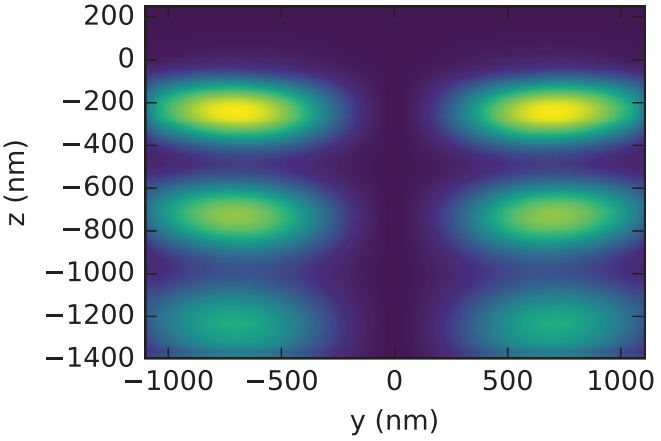

FIG. 12. The electric field intensity of the optical ring trap over the Au nanoplate shown in the y-z plane bisecting the ring trap. The surface of the Au nanoplate is at 0 nm. The maximum intensity of the first antinode occurs about 250 nm above the Au nanoplate mirror.

b. Van der Waals attractive forces

The nonretarded van der Waals potential energy of a sphere with a surface for all separations is [69]

$$W_{\mathrm{A}}(d) = -\frac{A}{6}\left(\frac{r}{d} + \frac{r}{2r+d} + \ln\frac{d}{2r+d}\right), \tag{D2}$$

where A is the Hamaker constant and r is the radius of the sphere. Lifshitz theory treats the objects as continuous materials with bulk refractive index and permittivity. The Hamaker constant for material 1 interacting with material 2 through material 3 is [70,71]

$$A = \frac{3k_{\mathrm{B}}T}{4}\left(\frac{\epsilon_1-\epsilon_3}{\epsilon_1+\epsilon_3}\right)\left(\frac{\epsilon_2-\epsilon_3}{\epsilon_2+\epsilon_3}\right) + \frac{3h}{4\pi}\int_{\nu_1}^{\infty}\frac{[\epsilon_1(i\nu)-\epsilon_3(i\nu)][\epsilon_2(i\nu)-\epsilon_3(i\nu)]}{[\epsilon_1(i\nu)+\epsilon_3(i\nu)][\epsilon_2(i\nu)+\epsilon_3(i\nu)]}\,d\nu, \tag{D3}$$

where ϵ_1, ϵ_2, and ϵ_3 are the electric permittivities of material 1, 2, and 3, respectively while $\epsilon_1(i\nu)$, $\epsilon_2(i\nu)$, $\epsilon_3(i\nu)$ are the permittivities at imaginary frequencies $i\nu$ (see Israelachvili [72] for more details), and $\nu_1 = 2\pi k_{\mathrm{B}}T/h = 3.9\times10^{13}$ Hz at 298 K. The permittivities at imaginary frequencies are calculated differently depending whether the material is dielectric or metallic [72]:

$$\epsilon_{\mathrm{dielectric}}(i\nu) = 1 + \frac{n^2-1}{1-(i\nu)^2/\nu_e^2}, \tag{D4a}$$

$$\epsilon_{\mathrm{metal}}(i\nu) = 1 - \nu_e^2/(i\nu)^2, \tag{D4b}$$

where n is the refractive index of the material and ν_e is the mean ionization frequency.

c. Double layer repulsive forces

The potential for the interaction of the double layer repulsion of a sphere with a surface is [73]

$$W_{\mathrm{R}}(d) = 16e^{-\kappa d}\epsilon r\left(\frac{k_{\mathrm{B}}T}{ze}\right)^2 \tanh\left(\frac{ze\psi_p}{4k_{\mathrm{B}}T}\right)\tanh\left(\frac{ze\psi_s}{4k_{\mathrm{B}}T}\right), \tag{D5}$$

where ϵ is the dielectric constant of the fluid, r is the radius of the sphere, $k_{\mathrm{B}}T$ is the thermal energy, z is the ion valency (assuming a symmetric electrolyte), e is the protonic charge, κ is the inverse Debye length, and ψ_s and ψ_p are the surface potentials of the sphere and the plate, respectively. The surface potential of the glass surface was estimated from Sze *et al.* [74] while the surface potential of an Ag nanoparticle was found experimentally through a ζ potential measurement [75]. The parameters used are in Eq. (D5): radius, $r = 75$ nm, $\epsilon = 80.4$, $\epsilon_0 = 8.85 \times 10^{-12}$ F m^{-1}, $e = 1.602 \times 10^{-19}$ C, $z = 1$, ionic strength, $I = 1.8 \times 10^{-4}$ mol L^{-1}, $\kappa = 4.4 \times 10^{7}$ m^{-1}, $\psi_s = -16$ mV, $\psi_p = -77$ mV.

2. Gravity contribution

The potential energy for gravity in this system decreases as a function of the particle's distance from the plate. This is because of the geometry of the experiment such that the coverslip is above and the particles are pushed up against it. The potential energy of gravity is

$$W_{\mathrm{g}}(d) = -\frac{4}{3}\pi r^3(\rho_{\mathrm{Ag}} - \rho_{\mathrm{H_2O}})gd, \tag{D6}$$

where $\rho_{\mathrm{Ag}} = 10.5$ g/cm^3, $\rho_{\mathrm{H_2O}} = 1.0$ g/cm^3, $g = 9.8$ m/s^2.

3. Laser contribution

The optical trap contributes two forces to the trapped spherical particle: the scattering force (along the optical axis) and the intensity gradient force. When the particle being trapped is much smaller than the wavelength of light ($R < \lambda/10$) the Rayleigh approximation holds, which treats the particle as a dipole affected by the electric field. For simplicity we will use the Rayleigh approximation for this calculation even though the particle radius is 75 nm compared to the wavelength in water being 800 nm/1.33 $\simeq$ 600 nm.

The scattering force is the result of photons scattering off the particle and imparting momentum to the particle. In the Rayleigh regime the scattering force is [76]

$$F_{\mathrm{scat}} = n_m\frac{\sigma\langle S\rangle}{c}, \tag{D7}$$

where σ is the particle's cross section defined as

$$\sigma = \frac{8}{3}\pi(kr)^4r^2\left(\frac{n^2-1}{n^2+2}\right)^2 \tag{D8}$$

and $\langle S\rangle$ is the time averaged Poyting vector. For a plane wave this is

$$\langle S\rangle = \frac{E_m^2}{2c\mu_o} = \frac{1}{2}E_m^2(c\epsilon_o), \tag{D9}$$

where E_m^2 is the intensity of the plane wave incident on the particle. The intensity can be estimated based on the power entering the microscope divided by the area of laser focus. The laser power is measured to be 112 mW after the SLM but before its microscope objective. The power lost from the objective transmission is estimated from the Olympus website and accounts for overfilling the back aperture. The area the laser illuminates is estimated from the diameter of the ring trap with diffraction limited annular width. For the experiments presented the power density is estimated to be 2.79×10^{-6} mW/nm^2. The wave vector is $k = 2\pi/\lambda$ where λ is the wavelength of the laser. Refractive indices for water at 800 nm is $n_{\mathrm{H_2O}} = 1.3290$ [77] and $n_{\mathrm{Ag}} = 0.0368$ for Ag [78]. The potential energy from the laser becomes

$$W_{\mathrm{scat}}(d) = F_{\mathrm{scat}} \times d. \tag{D10}$$

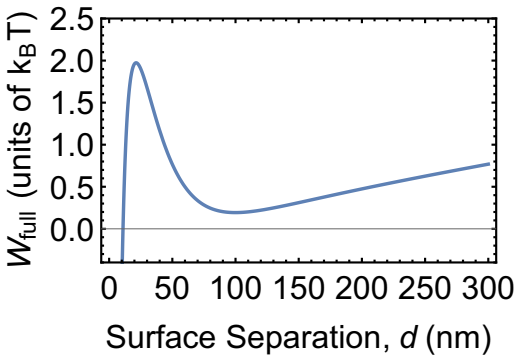

FIG. 13. The calculated potential energy of a Ag nanoparticle in an optical ring vortex over the glass surface. The minimum is at ~95 nm, and the barrier for the particle to spontaneously jump and get stuck on the glass surface is $\sim 1.8k_{\mathrm{B}}T$.

4. Total potential energy for the Ag nanoparticle near glass surface

The sum of all potentials [from Eqs. (D2), (D5), (D6), and (D10)] gives the full potential energy function of the 150-nm-diameter particle,

$$W_{\mathrm{full}}(d) = W_{\mathrm{A}}(d) + W_{\mathrm{R}}(d) + W_{\mathrm{g}}(d) + W_{\mathrm{scat}}(d). \tag{D11}$$

The potential energy function for the parameters given above is shown in Fig. 13. The minimum of this function will be the equilibrium position of the Ag nanoparticle near the glass surface.

APPENDIX E: FLUCTUATIONS INCREASE WITH INCREASING DRIVE FORCE

We present a series of simple analytical arguments that qualitatively explain increased fluctuations as a function of the driving force. As in the detailed numerical analysis, we imagine a system of two driven particles confined to a ring. The over-damped equations for motion of this pair of particles have the form

$$\frac{d\theta_{1/2}}{dt} = v_d - \mu V'(\theta_1,\theta_2) + \eta_{1/2}(t), \tag{E1}$$

where θ_i denotes the angular location of particle $i = \{1,2\}$, v_d is the driving force on the two particles, $V'(\theta_1,\theta_2)$ is the optical force of interaction between the two particles, and η_i

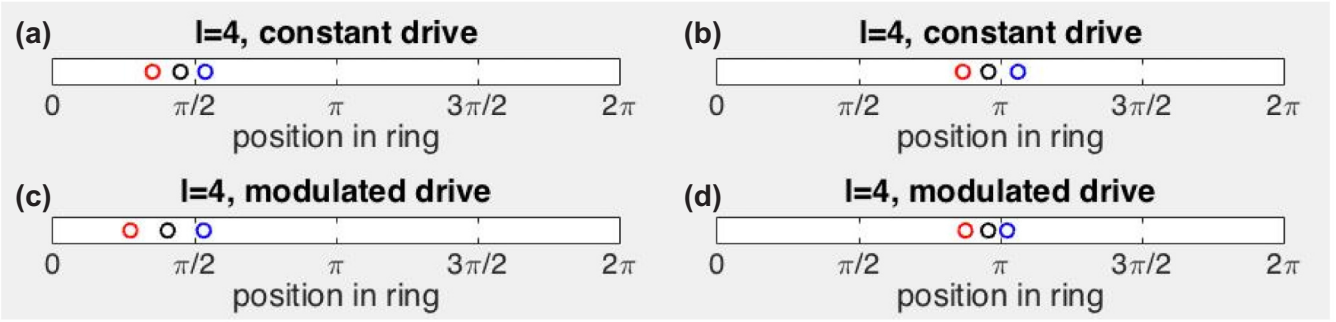

FIG. 14. Snapshots of the LD simulations for $l = 4$ for (a), (b) constant and (c), (d) modulated drive forces. Panels (a) and (b) show the positions of the particles in a constant drive force when the particles are located at $\pi/2$ (a) and π (b). Panels (c) and (d) show the positions of the particles in a modulated drive force when the particles are located at $\pi/2$ (c) and π (d). The angles correspond to the polar coordinate system used in the main text.

denotes the random noise term. Since we are interested in the potential of mean force for $\theta_1 - \theta_2$, we use Eq. (E1) to construct equations of motion for $\delta\theta = (\theta_1 - \theta_2)$ and $\theta_{\rm sum} = (\theta_1 + \theta_2)/2$,

$$\frac{d\delta\theta}{dt} = -2\mu V'(\theta_1,\theta_2) + 2\eta_-, \tag{E2}$$

$$\frac{d\theta_s}{dt} = v_d + \eta_+, \tag{E3}$$

where $\eta_\pm \equiv (\eta_1 \pm \eta_2)/2$ and we have used the fact that the forces on the particles due to the interparticle potential have opposite signs to derive Eq. (E2). To proceed, we will make the simplifying approximation that the two particle potential $V(\theta_1,\theta_2)$ depends simply on θ_s and $\delta\theta$, $V(\theta_1,\theta_2) \equiv \tilde{V}(\delta\theta,\theta_s)$.

This set of coupled equations can be simplified further by using the approximation $\theta_s(t) \approx v_d t$. With this approximation, we can view the time dependent two particle system with spatial modulation as a time dependent one particle problem without spatial modulation. This time dependent problem becomes analytically tractable in the limit of high driving force [58]. In this limit, the probability distribution for observing a certain $\delta\theta$ can be simply written as

$$P(\delta\theta) \sim e^{-\alpha \int_0^{2\pi} \tilde{V}(\delta\theta,x)dx}. \tag{E4}$$

The effective potential is simply the average of the potential $\tilde{V}$. This averaging can wash out some of the features of the strong time independent PMF and is the reason for larger fluctuations at higher drives.

1D Langevin dynamics (LD) simulations are discussed in the main text where the effects of a modulated drive force and interparticle potential were examined as a mechanism for the increased interparticle separation fluctuations. The changes in the interparticle separations are seen in snapshots of these LD simulations shown in Fig. 14 (see Supplemental Material [51] movie S6 for the full simulation). For LD simulations where the drive force is constant the relative positions of the particles remain approximately the same regardless of where the particles are located in the ring trap [Figs. 14(a) and 14(b)]. When the drive force is assumed to be modulated the interparticle separations increase [Fig. 14(c)] when they are in the ring trap at the $\pi/2$ and $3\pi/2$ positions for high drive. Likewise, the interparticle distances decrease [Fig. 14(d)] when they are at the 0 and π positions in the ring for low drive. The interparticle potential is modulated in both simulations. It is clear that the modulation in drive force, as opposed to the modulation of interparticle potential, is the dominant cause of the increase in fluctuations of interparticle separation.

[1] M. Reichert and H. Stark, J. Phys.: Condens. Matter **16**, S4085 (2004).
[2] Y. Sokolov, D. Frydel, D. G. Grier, H. Diamant, and Y. Roichman, Phys. Rev. Lett. **107**, 158302 (2011).
[3] J. Pesic, J. Z. Terdik, X. Xu, Y. Tian, A. Lopez, S. A. Rice, A. R. Dinner, and N. F. Scherer, Phys. Rev. E **86**, 031403 (2012).
[4] S. Okubo, S. Shibata, Y. S. Kawamura, M. Ichikawa, and Y. Kimura, Phys. Rev. E **92**, 032303 (2015).
[5] E. Lauga and T. R. Powers, Rep. Prog. Phys. **72**, 096601 (2009).
[6] T. Vicsek and A. Zafeiris, Phys. Rep. **517**, 71 (2012).
[7] M. C. Marchetti, J. F. Joanny, S. Ramaswamy, T. B. Liverpool, J. Prost, M. Rao, and R. A. Simha, Rev. Mod. Phys. **85**, 1143 (2013).
[8] J. Palacci, S. Sacanna, A. P. Steinberg, D. J. Pine, and P. M. Chaikin, Science **339**, 936 (2013).
[9] Y. Roichman, B. Sun, Y. Roichman, J. Amato-Grill, and D. G. Grier, Phys. Rev. Lett. **100**, 013602 (2008).
[10] Z. Yan, M. Sajjan, and N. F. Scherer, Phys. Rev. Lett. **114**, 143901 (2015).
[11] O. M. Marago, P. H. Jones, P. G. Gucciardi, G. Volpe, and A. C. Ferrari, Nat. Nanotechnol. **8**, 807 (2013).
[12] R. A. Beth, Phys. Rev. **50**, 115 (1936).
[13] L. Allen, M. W. Beijersbergen, R. J. C. Spreeuw, and J. P. Woerdman, Phys. Rev. A **45**, 8185 (1992).
[14] M. Dienerowitz, M. Mazilu, P. J. Reece, T. F. Krauss, and K. Dholakia, Opt. Express **16**, 4991 (2008).
[15] L. Tong, V. D. Miljkovic, and M. Käll, Nano Lett. **10**, 268 (2010).
[16] Z. Yan and N. F. Scherer, J. Phys. Chem. Lett. **4**, 2937 (2013).
[17] M. Nieto-Vesperinas, Phys. Rev. A **92**, 023813 (2015).
[18] J. E. Curtis and D. G. Grier, Phys. Rev. Lett. **90**, 133901 (2003).

[19] H. He, M. E. J. Friese, N. R. Heckenberg, and H. Rubinsztein-Dunlop, Phys. Rev. Lett. **75**, 826 (1995).
[20] K. T. Gahagan and G. A. Swartzlander, Opt. Lett. **21**, 827 (1996).
[21] M. E. J. Friese, J. Enger, H. Rubinsztein-Dunlop, and N. R. Heckenberg, Phys. Rev. A **54**, 1593 (1996).
[22] N. B. Simpson, K. Dholakia, L. Allen, and M. J. Padgett, Opt. Lett. **22**, 52 (1997).
[23] L. Paterson, M. P. MacDonald, J. Arlt, W. Sibbett, P. E. Bryant, and K. Dholakia, Science **292**, 912 (2001).
[24] K. Ladavac and D. G. Grier, Opt. Express **12**, 1144 (2004).
[25] K. Ladavac and D. G. Grier, Europhys. Lett. **70**, 548 (2005).
[26] S. H. Tao, X.-C. Yuan, J. Lin, and Y. Y. Sun, J. Appl. Phys. **100**, 043105 (2006).
[27] R. Di Leonardo, S. Keen, J. Leach, C. D. Saunter, G. D. Love, G. Ruocco, and M. J. Padgett, Phys. Rev. E **76**, 061402 (2007).
[28] Y. Roichman, D. G. Grier, and G. Zaslavsky, Phys. Rev. E **75**, 020401 (2007).
[29] S. H. Simpson and S. Hanna, J. Opt. Soc. Am. A **26**, 625 (2009).
[30] J. Ng, Z. Lin, and C. T. Chan, Phys. Rev. Lett. **104**, 103601 (2010).
[31] A. Lehmuskero, Y. Li, P. Johansson, and M. Käll, Opt. Express **22**, 4349 (2014).
[32] M. Li, S. Yan, B. Yao, Y. Liang, and P. Zhang, Opt. Express **24**, 20604 (2016).
[33] J. Kotar, M. Leoni, B. Bassetti, M. C. Lagomarsino, and P. Cicuta, Proc. Natl. Acad. Sci. USA **107**, 7669 (2010).
[34] Y. Sassa, S. Shibata, Y. Iwashita, and Y. Kimura, Phys. Rev. E **85**, 061402 (2012).
[35] H. Nagar and Y. Roichman, Phys. Rev. E **90**, 042302 (2014).
[36] A. S. Ostrovsky, C. Rickenstorff-Parrao, and V. Arrizón, Opt. Lett. **38**, 534 (2013).
[37] M. Chen, M. Mazilu, Y. Arita, E. M. Wright, and K. Dholakia, Opt. Lett. **38**, 4919 (2013).
[38] M. M. Burns, J. M. Fournier, and J. A. Golovchenko, Phys. Rev. Lett. **63**, 1233 (1989).
[39] P. C. Chaumet and M. Nieto-Vesperinas, Phys. Rev. B **64**, 035422 (2001).
[40] S. A. Tatarkova, A. E. Carruthers, and K. Dholakia, Phys. Rev. Lett. **89**, 283901 (2002).
[41] S. Mohanty, J. Andrews, and P. Gupta, Opt. Express **12**, 2746 (2004).
[42] D. S. Bradshaw and D. L. Andrews, Phys. Rev. A **72**, 033816 (2005).
[43] K. Dholakia and P. Zemánek, Rev. Mod. Phys. **82**, 1767 (2010).
[44] O. Brzobohatý, T. Čižmár, V. Karásek, M. Šiler, K. Dholakia, and P. Zemánek, Opt. Express **18**, 25389 (2010).
[45] V. Demergis and E. L. Florin, Nano Lett. **12**, 5756 (2012).
[46] Z. Yan, R. A. Shah, G. Chado, S. K. Gray, M. Pelton, and N. F. Scherer, ACS Nano **7**, 1790 (2013).
[47] Z. Yan, Y. Bao, U. Manna, R. A. Shah, and N. F. Scherer, Nano Lett. **14**, 2436 (2014).
[48] M. M. Burns, J. M. Fournier, and J. A. Golovchenko, Science **249**, 749 (1990).
[49] N. Sule, S. A. Rice, S. K. Gray, and N. F. Scherer, Opt. Express **23**, 29978 (2015).
[50] Y. Roichman and D. G. Grier, Proc. SPIE **6483**, 64830F (2007).
[51] See Supplemental Material at http://link.aps.org/supplemental/10.1103/PhysRevE.95.022604 for videos that correspond to experimental data and simulation results.
[52] D. B. Ruffner and D. G. Grier, Phys. Rev. Lett. **111**, 059301 (2013).
[53] W. Mu, Z. Liu, L. Luan, G. Wang, G. C. Spalding, and J. B. Ketterson, New J. Phys. **11**, 103017 (2009).
[54] M. Bandyopadhyay, S. Dattagupta, and M. Sanyal, Phys. Rev. E **73**, 051108 (2006).
[55] T. Li, in *Fundamental Tests of Physics with Optically Trapped Microspheres* (Springer, New York, 2013), pp. 9–21.
[56] M. A. Bevan and D. C. Prieve, J. Chem. Phys. **113**, 1228 (2000).
[57] Z. Yan, S. K. Gray, and N. F. Scherer, Nat. Commun. **5**, 3751 (2014).
[58] P. Reimann, R. Bartussek, R. Häußler, and P. Hänggi, Phys. Lett. **A215**, 26 (1996).
[59] P. Reimann, C. Van den Broeck, H. Linke, P. Hänggi, J. M. Rubi, and A. Pérez-Madrid, Phys. Rev. E **65**, 031104 (2002).
[60] S. H. Lee and D. G. Grier, Phys. Rev. Lett. **96**, 190601 (2006).
[61] M. Evstigneev, O. Zvyagolskaya, S. Bleil, R. Eichhorn, C. Bechinger, and P. Reimann, Phys. Rev. E **77**, 041107 (2008).
[62] S. Albaladejo, M. I. Marqués, F. Scheffold, and J. J. Sáenz, Nano Lett. **9**, 3527 (2009).
[63] M. Khoury, A. M. Lacasta, J. M. Sancho, and K. Lindenberg, Phys. Rev. Lett. **106**, 090602 (2011).
[64] P. Reimann, C. Van den Broeck, H. Linke, P. Hänggi, J. M. Rubi, and A. Pérez-Madrid, Phys. Rev. Lett. **87**, 010602 (2001).
[65] I. F. Sbalzarini and P. Koumoutsakos, J. Struct. Biol. **151**, 182 (2005).
[66] W. Sun, S. Pan, and Y. Jiang, J. Mod. Opt. **53**, 2691 (2006).
[67] S. C. Kong, J. J. Simpson, and V. Backman, IEEE Microw. Wirel. Compon. Lett. **18**, 4 (2008).
[68] H.-J. Butt, K. Graf, and M. Kappl, *Physics and Chemistry of Interfaces*, 2nd revised ed. (Wiley-VCH, Weinheim, FRG, 2006), pp. 80–117.
[69] H. C. Hamaker, Physica **4**, 1058 (1937).
[70] E. Lifshitz and M. Hamermesh, *Perspectives in Theoretical Physics* (Pergamon, 1992), Chap. 26, pp. 329–349.
[71] I. Dzyaloshinskii, E. Lifshitz, and L. Pitaevskii, Adv. Phys. **10**, 165 (1961).
[72] J. N. Israelachvili, *Intermolecular and Surface Forces*, rev. 3rd. ed. (Elsevier, Waltham, MA, 2011), Chap. 13, pp. 253–289.
[73] S. G. Flicker, J. L. Tipa, and S. G. Bike, J. Colloid Interface Sci. **158**, 317 (1993).
[74] A. Sze, D. Erickson, L. Ren, and D. Li, J. Colloid Interface Sci. **261**, 402 (2003).
[75] A. D. Mcnaught and A. Wilkinson, *IUPAC Compendium of Chemical Terminology*, 2nd ed. (IUPAC, Research Triangle Park, NC, 1997).
[76] G. Gouesbet, B. Maheu, and G. Gréhan, J. Opt. Soc. Am. A **5**, 1427 (1988).
[77] G. M. Hale and M. R. Querry, Appl. Opt. **12**, 555 (1973).
[78] P. B. Johnson and R. W. Christy, Phys. Rev. B **6**, 4370 (1972).